3-dimensional particle image velocimetry based evaluation of turbulent skin-friction reduction by spanwise wall oscillation

Kempaiah, Kushal U.; Scarano, Fulvio; Elsinga, Gerrit E.; Van Oudheusden, Bas W.; Bermel, Leon

Important note
To cite this publication, please use the final published version (if applicable).
Please check the document version above.

Kushal U. Kempaiah, Fulvio Scarano, Gerrit E. Elsinga, Bas W. van Oudheusden, and Leon Bermel

View Online   Export Citation   CrossMark

ARTICLES YOU MAY BE INTERESTED IN

Passive and active control of turbulent flows
Physics of Fluids **32**, 080401 (2020); https://doi.org/10.1063/5.0022548
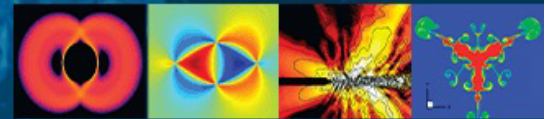
Frameworks for investigation of nonlinear dynamics: Experimental study of the turbulent jet
Physics of Fluids **32**, 085112 (2020); https://doi.org/10.1063/5.0014939

Lift enhancement strategy and mechanism for a plunging airfoil based on vortex control
Physics of Fluids **32**, 087116 (2020); https://doi.org/10.1063/5.0019317

Physics of Fluids
GALLERY OF COVERS

AIP Publishing

3-dimensional particle image velocimetry based evaluation of turbulent skin-friction reduction by spanwise wall oscillation

Kushal U. Kempaiah,[a]) 🆔   Fulvio Scarano, 🆔   Gerrit E. Elsinga, 🆔   Bas W. van Oudheusden, 🆔 and Leon Bermel 🆔

AFFILIATIONS

Delft University of Technology, Delft, The Netherlands

[a])Author to whom correspondence should be addressed: k.ujjainikempaiah@tudelft.nl

ABSTRACT

The reduction of turbulent skin-friction drag and the response of vortical structures in a zero-pressure gradient, turbulent boundary layer subjected to spanwise wall oscillation is investigated using planar and tomographic particle image velocimetry (PIV). The experiments are conducted at a momentum based Reynolds number of 1000, while the range of spanwise oscillation amplitude and frequency is chosen around the optimum reported in previous studies. A high-resolution planar PIV measurement is employed to determine the drag reduction directly from wall shear measurements and to analyze the accompanying modifications in the turbulent vortical structures. Drag reduction of up to 15% is quantified, with variations following the trends reported in the literature. The analysis of the turbulence structure of the flow is made in terms of Reynolds shear stresses, turbulence production, and vortex visualization. A pronounced drop of turbulence production is observed up to a height of 100 wall units from the wall. The vorticity analysis, both in the streamwise wall-normal plane and in the volumetric results, indicates a reduction of vorticity fluctuations in the near-wall domain. A distortion of the hairpin-packet arrangement is hypothesized, suggesting that the drag-reduction mechanism lies in the inhibition of the hairpin auto-generation by the spanwise wall oscillations.

NOMENCLATURE

Symbols

A_{osc}^+	amplitude of oscillations
C_f^0	skin-friction coefficient of stationary wall
C_f	skin-friction coefficient of oscillating wall
d_p	diameter of tracer particles
f	frequency of oscillation
$f_\#$	imaging f-stop
H	boundary layer shape factor
L	length of oscillating plate
l^+	length of one wall unit
M	optical magnification
N	number of samples
Re_θ	Reynolds number based on momentum thickness
Re_τ	Reynolds number based on wall friction velocity
T_{osc}^+	time-period of oscillations
t_{auto}^+	Hairpin auto-generation time

U_∞	freestream velocity
$\bar{u}$	mean velocity
u_τ	wall friction velocity
W_m^+	oscillating wall velocity
x	streamwise coordinate
y	wall normal coordinate
z	spanwise coordinate
δ_{st}^+	stokes layer thickness
δ^*	displacement thickness
δ_{99}	boundary layer thickness
$\epsilon_{\bar{u}}$	uncertainty of mean velocity
$\epsilon_{u'}$	uncertainty of fluctuations
θ	momentum thickness
ν	kinematic viscosity
τ_w	shear stress at the wall
ϕ	phase of the oscillating wall
ω_z^+	vorticity fluctuation
$\omega^{\bar{2}}$	enstrophy
$+$	inner scaling

Abbreviations

DNS	direct numerical simulations
DR	drag reduction
HWA	hot wire anemometry
L2	lambda-2 criterion
PIV	particle image velocimetry
ppp	particles per pixel
TKE	Turbulent kinetic energy

I. INTRODUCTION

Turbulent skin-friction drag is relevant to a multitude of natural processes and engineering applications and has been widely studied. Several attempts to control turbulent drag have been reported using both passive and active techniques (Gad-el-Hak, 1996). Early studies of turbulent boundary layers (Driver and Hebbar, 1987 and Howard and Sandham, 2000) showed that a fully developed turbulent boundary layer when subjected to a sudden spanwise pressure gradient resulted in the reduction of turbulence production and Reynolds stresses. The Direct Numerical Simulation (DNS) study of Sendstad and Moin (1992) showed that skewing motion is necessary to weaken the quasi-streamwise vortices. Following this, spanwise wall oscillations received much attention, given the potential to achieve a significant skin-friction reduction.

The first studies reported by Jung et al. (1992), who performed a DNS of the flow in a rectangular channel at Re_τ = 200, indicated reductions as high as 40%, where Re_τ is the Reynolds number based on the wall friction velocity u_τ. Experiments conducted by Laadhari et al. (1994) provided support to the numerical studies. Following these early studies, several numerical (Baron and Quadrio, 1995; Quadrio and Sibilla, 2000; and Choi et al., 2002) and experimental investigations (Choi, 2002 and Di Cicca et al., 2002) have been performed. Reductions of 45% in skin friction (Quadrio and Ricco, 2004) have been reported at optimum conditions. The parameters that characterize the imposed spanwise wall oscillation are its amplitude Z_{osc} and time period T_{osc} expressed in the non-dimensional form (T_{osc}^+ and Z_{osc}^+, respectively) through u_τ and the kinematic viscosity ν. It should be noted, however, that not all oscillation regimes lead to a reduction in drag. The current literature states that the oscillations corresponding to $T_{osc}^+ \approx 100$ lead to maximum skin-friction drag reduction when A_{osc}^+ exceeds 100, which corresponds to the mean streak spacing (Kline et al., 1967). Further increasing the amplitude produces even higher drag reduction. Concerning the physical mechanisms of drag reduction, it has been proposed that the imposed spanwise wall motion affects the orientation of the streamwise vortices, in turn, disrupting the lift-up mechanism, and thereby the production of turbulence (Di Cicca et al., 2002; Touber and Leschziner, 2012). This directly corresponds to a reduction in the ejection and sweep events, which are the drivers for wall-normal momentum transport. These ejections are associated with the formation of hairpin or horseshoe vortices (Zhou et al., 1999; Christensen and Adrian, 2001), which are known to occur in packets and travel with similar velocities (Adrian et al., 2000).

A solitary hairpin vortex is a coherent structure that explains many characteristics observed in wall-bounded turbulent flows (Robinson, 1991; Adrian, 2007). However, due to the non-linear behavior of the flow dynamics, coherent structures are typically not symmetric, as the hairpin, but rather asymmetric and "cane" shaped vortices have also been observed. Subsequent work (Adrian et al., 2000) on turbulent boundary layers has shown that multiple hairpins originate from near the wall over the low-speed streaks and grow as they develop to then populate the entire boundary layer, giving rise to what is termed a hairpin packet. It is therefore of interest to understand and quantify the effect of spanwise wall oscillations on these coherent structures and the hairpin packets.

Although both DNS and experiments have provided evidence that spanwise oscillations can lead to a reduction in skin-friction drag, there are many quantitative discrepancies when comparing the maximum drag reduction that is observed, as noted by Quadrio and Ricco (2004). A possible contributing factor to these differences is the low value of the Reynolds number at which numerical studies are conducted when compared to experiments. Ricco and Quadrio (2008) analyzed the effect of Reynolds number on the drag reduction, reporting a drop by 5% as Re_τ was increased from 200 to 400. This result brought the effect of the Reynolds number on the mechanism responsible for the drag reduction to the attention of researchers. Reynolds number effects were scrutinized up to Re_τ = 1000 by Touber and Leschziner (2012), who also concluded that the large-scale structures in the outer layer affect the near-wall dynamics and associated skin friction reduction. This mechanism helps explain the dependence upon the Reynolds number. Moreover, it is suggested that the flow behavior also depends upon the flow configuration, with turbulent large-scale structures in external flows (boundary layers) differing from those observed in channel flows, especially at higher values of the Reynolds number (Monty et al., 2009). Moreover, large-scale wall-attached structures surpass the centerline affecting the opposite wall in a channel (Lozano-Durán et al., 2012). These differences are important when comparing numerical simulations with experiments because the former mostly concern channel flow (Quadrio and Ricco, 2004; Touber and Leschziner, 2012), while the experimental studies more often deal with boundary layers (Choi et al., 1998; Choi, 2002; and Di Cicca et al., 2002).

Experiments on drag reduction by spanwise wall oscillations reported in the literature have widely employed hot wire anemometry (HWA), given the high accuracy, small probe size, and the high temporal resolution. It is beneficial for extracting spectral information, single-probe HWA measurements do not provide complete information on the behavior of the different components of the Reynolds stresses, for which it is important to quantify the change in velocity fluctuations in both the streamwise and wall-normal directions within the boundary layer, which are connected to the turbulent shear stress and wall-normal momentum transport. In addition, turbulent kinetic energy (TKE) production, which is related to the shear stress, can also explain the effects of the wall oscillation. Knowledge of the Reynolds stresses would require multi-wire probes and for the study of the velocity gradient components (e.g., vorticity) multi-wire arrays (Vukoslavĉević et al., 1991). Measurements with planar particle image velocimetry (PIV) provide quantitative information on the in-plane components of the Reynolds stress tensor as well as the spanwise component of the vorticity vector (Adrian et al., 2000) at a high resolution. The high-resolution data allow us to directly measure the local shear at the wall, provided that the spatial resolution matches the scale of the viscous layer (Kähler et al., 2006) and is also used to describe relevant properties in the boundary
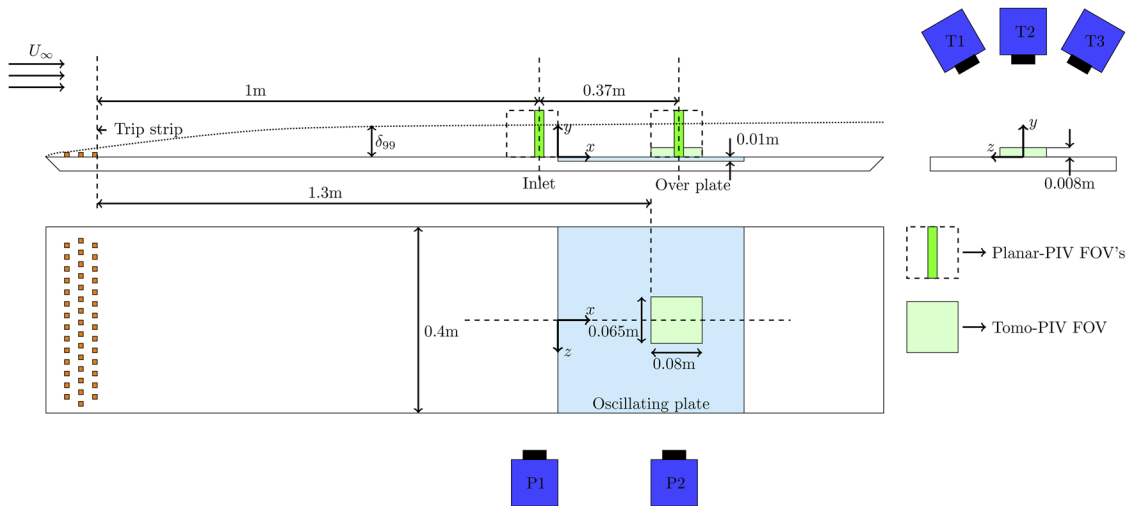
FIG. 1. Schematic of the oscillating plate setup with acquisition locations for both planar and tomographic measurements shown (not to scale).

layer such as the turbulent kinetic energy production and Reynolds shear stress (Kline *et al.*, 1967). Direct measurement of wall shear by PIV has not yet been attempted for the spanwise oscillating wall problem because of the spatial resolution limits encountered in past experiments (Di Cicca *et al.*, 2002). The lack of data in three dimensions (3D) is overcome by employing tomographic PIV (Elsinga *et al.*, 2006), which provides information on the instantaneous 3D organization of the coherent structures in the turbulent boundary layer.

The present study describes the application of planar and tomographic PIV to study skin-friction drag reduction over a spanwise oscillating wall. The drag estimates are obtained employing high-resolution planar PIV to measure the near-wall velocity gradient, yielding an estimate of the wall shear. The method and its inherent uncertainties are discussed, and the findings are compared with existing data. The vortex dynamics in the boundary layer are investigated through vorticity analysis and by observing the instantaneous planar and 3D vorticity fields, which are used to infer the organization of the turbulent structures, with a focus on hairpin packets and the modifications incurring when spanwise oscillations induce drag reduction.

II. EXPERIMENTAL SETUP AND PROCEDURE

A. Wind tunnel and oscillating wall

The experiments were conducted in an open-return low-speed wind tunnel at the Aerospace Engineering laboratories of the Delft University of Technology. The tunnel features a contraction ratio of 9:1 with an exit cross section of 40×40 cm^2. The flow at the exit was confined within a 1.6 m long rectangular channel and a flat plate is installed 0.1 m above the channel floor. For the current experimental conditions, the turbulence intensity at the edge of the boundary layer was measured to be below 1.4%.

The boundary layer was tripped at a distance of 5 cm after the leading edge of the plate using distributed roughness elements of 1.0 cm height (Lima Pereira *et al.*, 2020). The schematic layout of the experiment is illustrated in Fig. 1. The oscillating plate has a streamwise length of $L = 0.4$ m and is installed 1.0 m downstream of the location where the boundary layer transition is forced. The oscillations were obtained using a slider–crank mechanism capable of reaching up to 15 Hz oscillation frequency and with a peak-to-peak amplitude of 2 cm. A counterweight was introduced in the oscillation mechanism to minimize vibrations. The test section was realized in Plexiglas to provide optical access for PIV illumination and imaging. The measurements were performed at a free stream velocity of 3.0 m/s, corresponding to a momentum-thickness-based Reynolds number $Re_\theta \sim 10^3$. The properties of the undisturbed incoming boundary layer, immediately upstream of the oscillating plate, are described in Table I, where Re_τ is the Reynolds number based on the friction velocity, U_∞ is the free stream velocity, δ_{99} is the boundary layer thickness, δ^* is the displacement thickness, θ is the momentum thickness, l^+ is the length of one wall unit, and H is the shape factor.

TABLE I. Boundary layer properties at $x = 1.0$ m from leading edge (Inlet, Fig. 1).

Re_θ	Re_τ	U_∞ (m/s)	δ_{99} (mm)	δ^* (mm)	θ (mm)	u_τ (m/s)	l^+ (mm)	H
980	570	3.0	59.0	6.7	4.9	0.145	0.10	1.36

B. Particle image velocimetry

The planar-PIV measurements were obtained using two LaVision *Imager sCMOS* cameras (2560×2160 pixels^2, 16 bits, and 6.5 μm pixel size) equipped with Nikon objectives of 105 mm focal length (P1 and P2, Fig. 1). The measurements were performed at two streamwise locations: ahead ($x/L = -0.075$) and over ($x/L = 0.85$) the oscillating plate, at the wall-normal (xy) positions indicated in (Fig. 1). The non-dimensionalization of the streamwise location is done with the length of the oscillating plate with its leading edge as reference. The flow was seeded with fog droplets of 1 μm diameter produced with a SAFEX smoke generator. Illumination was provided by a Quantel *Evergreen* 200 laser (Nd:YAG, 2×200 mJ, 15 Hz). The digital synchronization between laser, cameras, and the image acquisition system was provided by a LaVision programmable timing unit controlled through DaVis 8.4. The light sheet was 2 mm thick, oriented parallel to the flow, and aligned at the midplane through the reference axis providing measurements in the streamwise-wall normal plane. Hardware details and settings are listed in Table II.

The tomographic measurements were performed at a streamwise distance of $x/L = 0.75$ downstream from the leading edge of the oscillating plate. The measurement volume encompassed a region of 80 (x) $\times$ 65 (z) $\times$ 8 (y) mm^3, which corresponds to $800 \times 650 \times 80$ wall units over the surface of the oscillating wall, with the smallest dimension normal to the wall (Fig. 1). The fog particles were used to obtain a particle image density of $\sim$0.015 particles per pixel (ppp). The same illumination source was employed as for the planar experiment. A knife-edge slit was added to the path of the laser light sheet to obtain uniform light intensity over the measurement volume of 8 mm thickness above the wall. A dual-pass

illumination (Ghaemi and Scarano, 2010) was obtained with a planar mirror placed at the opposite side of the light entrance, which intensified laser illumination and homogenized the light received by the cameras partly in back- and forward-scattering mode. The tomographic imaging system featured four LaVision *imager sCMOS* cameras (T1, T2, and T3, Fig. 1). Three cameras subtended an arc with a total angle of 50°. The fourth camera monitored the position of the oscillating wall. The focal plane of each imaging unit was aligned with the median plane of the laser sheet by means of Scheimpflug adapters able to tilt the objectives relative to the image plane along oblique axes. The average imaging magnification was $M = 0.2$ with a digital resolution of 32 pixels/mm. The recording rate was 13.5 Hz and the time separation between subsequent exposures was set at 150 μs.

C. Data reduction and uncertainty analysis

For the planar-PIV measurements, the recorded sequences comprised 2000 double-frame images, with details given in Table II. The image interrogation was performed using multi-pass cross-correlation with window refinement and deformation (Scarano and Riethmuller, 2000). Non-isotropic windows were used to increase the wall-normal resolution (Scarano, 2003). In the final iterations, windows of 48×12 pixels^2 (1.41×0.35 mm^2) were used with an overlap factor of 75% (3:4) along the vertical direction. The resulting vector spacing was 0.081 mm (11.5 vec/mm) along the wall-normal direction, corresponding to approximately one wall unit (see Table I). The size of the correlation window for the visualization of velocity and vorticity was 32×32 pixels^2 (0.94×0.94 mm^2), with a vector pitch of 0.23 mm. The dynamic spatial range given as the ratio

TABLE II. Description of parameters for the PIV measurements.

	Planar-PIV	Tomographic-PIV
Seeding particles	Fog droplets ($d_p = 1$ μm)	
Illumination	Nd:YAG, 2×200 mJ, 15 Hz	
Recording device	sCMOS (2560×2160 pixels^2, 16 bits, 6.5 μm pixel pitch)	
Recording method	Double frame/Single exposure	
Number of cameras	2 (P1, P2)	3 (T1, T2, T3)
Field of view	7.4×6.2 cm^2	$8.0 \times 6.5 \times 0.8$ cm^3
Recording lens and aperture	105 mm, $f_\# = 8.0$	105 mm, $f_\# = 8.0$
Imaging resolution	30 pixels/mm	32 pixels/mm
Observation distance	0.4 m	0.4 m
Optical magnification	0.22	0.2
Image seeding density	0.03 ppp	0.015 ppp
Recording frequency	15 Hz (multiple acquisitions)	13.5 Hz
Pulse delay	150 μs	150 μs
Number of recordings	2000	100 (*at each phase*)
Interrogation window and vector pitch (wall shear meas.)	1.4×0.35 mm^2(48×12 *px*) (75% overlap along y) 0.081 mm	
Interrogation window and vector pitch (vorticity meas.)	0.94×0.94 mm^2(32×32 *px*) (75% overlap) 0.23 mm	$48 \times 48 \times 48$ voxels (75% overlap) 0.38 mm
Dynamic spatial range	180 (wall normal direction)	50
Dynamic velocity range	200	200

TABLE III. Statistical uncertainty of mean velocity and turbulent fluctuations at y^+ = 10 [% with respect to mean free-stream velocity ($\bar{u}$)].

Re_θ	Number of samples	Uncertainty mean $\epsilon_{\bar{u}}$ (%)	Uncertainty variance $\epsilon_{u'}$ (%)
980	2000	1.25	3.4

between the length of the measurement domain and the interrogation window (Adrian, 1997) was 180, considering the wall-normal direction. The dynamic velocity range given as the ratio of maximum velocity to the minimum resolvable velocity was 60, based on the diffraction limit criterion and the maximum particle displacement in the measurement domain (Adrian and Westerweel, 2011).

For the near-wall measurements, attention was posed first to accurately determine the position of the wall (Sec. II). Second, measurements within the viscous sub-layer ($y^+ < 5$) were obtained with five vectors in the first 0.5 mm, where the velocity was observed to follow a linear trend.

The measurement uncertainty of the velocity statistics was based on the convergence of the Gaussian dispersion based on 2000 uncorrelated samples. A 95% confidence interval was considered, according to Eqs. (1) and (2). The data are presented in Table III,

$$\epsilon_{\bar{u}} = \frac{1.96}{\bar{u}} \frac{\sigma_{\bar{u}}}{\sqrt{N-1}}, \tag{1}$$

$$\epsilon_{u'} = \frac{1.96}{\sqrt{N-1}}. \tag{2}$$

For the tomographic measurements, the object-to-image calibration was performed with a plate (LaVision *Type* 10) with 16 × 14 markings, imaged at three positions along the volume depth. After 3D self-calibration (Wieneke, 2008), the calibration disparity was reduced to ~0.02 pixels. The intensity distribution was reconstructed in a 80 × 65 × 8 mm³ volume, which corresponds to 800 × 650 × 80 in wall units discretized with 2580 × 2096 × 258 voxels using the CSMART reconstruction algorithm (Gan *et al.*, 2012) with five iterations. Image pre-processing was performed to remove background intensity by subtracting the minimum value of intensity at each pixel. The cross-correlation analysis returned 215 × 91 × 11 velocity vectors using an interrogation volume size of 48 × 48 × 48 voxels (1.5 mm linear size), yielding a vector spacing of 0.375 mm with 75% overlap (Table IV). For the case with the oscillating wall, specific values of the phase ϕ were examined, namely, that of maximum transverse wall velocity ($\phi = 0, \pi$) and that of maximum transverse displacement, when the motion is inverted (minimum velocity, $\phi = \pi/2, 3\pi/2$; Sec. III D).

TABLE IV. Tomographic reconstruction processing parameters.

Image pre-processing	Subtract time average pixel intensity
3D calibration	3rd order polynomial at 3 planes
Calibration correction	Volume self-calibration
Volume discretization	2580 × 2096 × 258 voxels
Reconstruction technique	CSMART (5 iterations)

When comparing the mean velocity profile from the tomo-PIV measurements to the high-resolution 2C-PIV and DNS data (Sec. III A), agreeing values in the range $20 < y^+ < 80$ were obtained. Closer to the wall, laser light reflections hampered the measurements. Also, above 80 wall units from the wall, the illumination laser light intensity decays and particles were not detectable. The data from tomographic PIV were employed primarily for vorticity analysis. The accuracy of the velocity gradient was estimated from the analysis of the measured velocity divergence (Scarano and Poelma, 2009). The conservation of mass necessitates the divergence of the velocity field to be zero in the domain. The distribution of the divergence exhibits a normal distribution around 0, with a standard deviation corresponding to 40 s⁻¹. Considering that instantaneous vorticity fluctuations are measured that attain a typical value of 200 s⁻¹ (see for instance, Sec. III E), the estimated relative uncertainty amounts to 20%. The errors are mostly ascribed to the truncation effects arising from the limited spatial resolution of the measurement, following the work of Scarano and Poelma (2009).

D. Drag reduction evaluation

The time-averaged velocity profile measured by planar PIV features a symmetric shape with respect to the wall: the data points "inside the wall" being the result of the reflections of particle tracers. The symmetry axis can, therefore, be used to indicate with good accuracy the position of the mirroring wall. Figure 2 illustrates the velocity profile in proximity of the wall. The vertical axis, in this case, represents the wall-normal coordinate, with an arbitrary point of origin. From the symmetry of the profile, the wall position was inferred to be at y = 2.47 mm, with an uncertainty of 0.01 mm estimated from the discrepancy between the two linear fit from above the wall and the reflected image, respectively.

The slope $\left(\frac{\partial u}{\partial y}\right)_{y=0}$ at the wall is estimated from a linear fit in the data interval from 0.15 mm to 0.4 mm ($y^+ = 1.5 - 4$), where the velocity exhibits a linear behavior within a correlation of 95%.
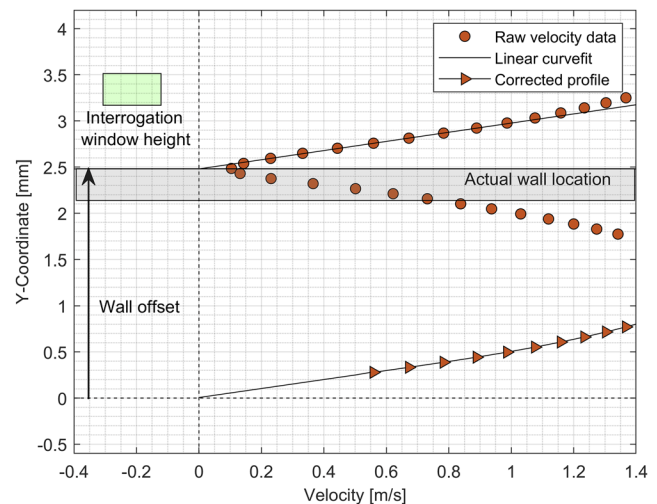

FIG. 2. Wall position determination at x = 1.37 m from the leading edge (over plate, Fig. 1).

The above provides a quantitative description of the shear stress τ_w, which is determined with an uncertainty of 1.5%. Accordingly, the friction velocity and skin-friction coefficient (C_f) are calculated as

$$u_\tau = \sqrt{\nu\left(\frac{\partial u}{\partial y}\right)}, \quad (3)$$

$$C_f = 2\left(\frac{u_\tau}{u_\infty}\right)^2. \quad (4)$$

Following the work of Quadrio and Ricco (2004), the drag reduction is defined as

$$\text{Drag reduction (DR)}(\%) = \frac{C_f^0 - C_f}{C_f^0} \times 100, \quad (5)$$

where C_f^0 and C_f are the skin friction on the steady and the oscillating wall, respectively.

III. RESULTS

A. Turbulent boundary layer characteristics

The mean boundary layer velocity profile and the kinematic Reynolds stresses at the inlet plane just upstream of the oscillation plate (see Fig. 1) were obtained by ensemble averaging of the PIV velocity data and represented in wall-unit scaling. The velocity profile is compared with DNS data computed at $Re_\theta = 1000$ and $Re_\tau = 360$ (Schlatter and Örlü, 2010). The planar PIV data exhibit a good agreement in the inner region with a resolved viscous sublayer (Sec. II C) as shown in the near-wall profile (inset Fig. 3). The spatial range of the tomographic measurements was fairly limited in the wall normal direction ($y^+ = [20 - 80]$), given that the tomographic data are intended to visualize the velocity and vorticity structures along the spanwise and streamwise directions. The reduced wake

region is attributed to the influence of the strong tripping that is employed [Vila *et al.* (2017)].

The Reynolds stresses obtained from 2C-PIV are in good agreement with the DNS data (Fig. 4) with peak streamwise fluctuations $\langle u'u' \rangle^+$ slightly higher than DNS by 2%. A small shift of the data toward higher y^+ is suggested, however, in the order of $1y^+$, which corresponds to the uncertainty in the location of the wall. The deviations observed in the outer regions of the boundary layer where the intensity of the measured fluctuations persists at $y^+ \sim 500$, whereas the DNS results collapse to zero already at $y^+ \sim 400$ due to the difference in Re_τ of the data.

B. Turbulent skin-friction analysis

The experiments were conducted for different values of the oscillation frequency and with a constant amplitude, following Table V. The range of imparted oscillatory motions covers both favorable and unfavorable conditions, and the trends are depicted in Fig. 5. A peak reduction of 15% is obtained at $T_{osc}^+ = 94$ and $A_{osc}^+ = 100$. The non-dimensional wall velocity ($W_m^+ = \pi A_{osc}^+/T_{osc}^+$) corresponding to the above case is $W_m^+ = 3.34$ and the reported reduction from the literature for a similar condition ($T_{osc}^+ = 100$ and $W_m^+ = 4.5$) is 17%, according to the work of Quadrio and Ricco (2004). From Table V, it can be observed that the oscillations lead to significant drag reduction in the range of $T_{osc}^+ = [94 - 175]$. The effects of the oscillating wall penetrate through the boundary layer up to a thickness estimated by $\delta_{st} = \sqrt{\frac{\nu}{\pi f}}$, and this region is denoted as the Stokes layer, in reference to the Stokes second problem (Schlichting and Gersten, 2016), where f is the frequency of oscillation. Table V contains the inner-scaled Stokes layer thickness for the investigated range of T_{osc}^+. Baron and Quadrio (1995) stated that a Stokes layer of thickness less than $10y^+$, associated with the region where streaks are more prevalent, results in drag reduction as long as the A_{osc}^+ is greater than 100, corresponding to the mean
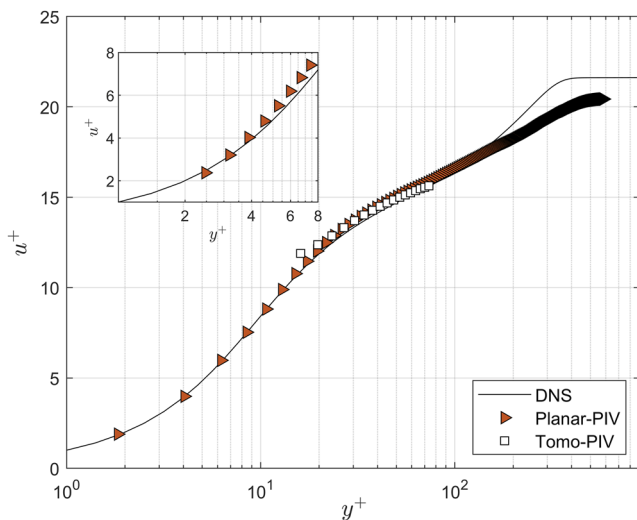

FIG. 3. Measured mean streamwise velocity profile for the stationary wall with inner-layer scaling and comparison to DNS data from the literature ($Re_\theta = 1000$).
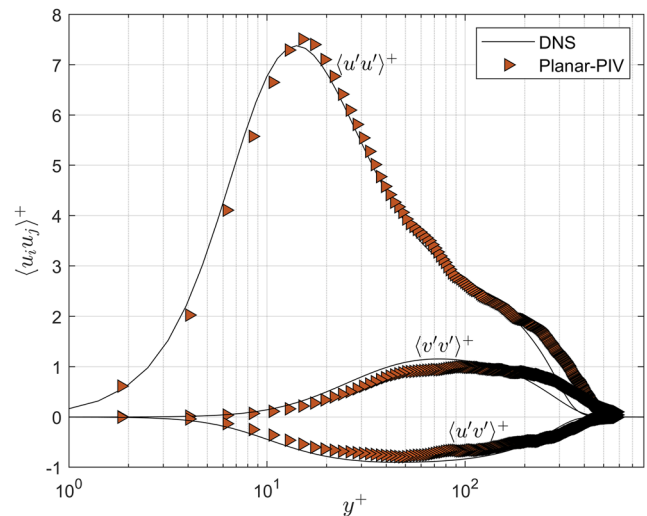

FIG. 4. Measured wall-normal profiles of Reynolds stresses for the stationary wall and comparison to DNS data from the literature ($Re_\theta = 1000$).

TABLE V. Drag reduction inferred from wall shear measurements for $Re_\theta = 1000$.

T_{osc}^+	A_{osc}^+	W_m^+	Stokes layer $\delta_{st}{}^+$	% DR ("+" indicates reduction)
94 (15 Hz)		3.34	5.5	+14.6
107 (13 Hz)		2.93	5.9	+9.9
140 (10 Hz)	100 (10 mm)	2.24	6.7	+8.7
175 (8 Hz)		1.79	7.5	+4.6
350 (4 Hz)		0.89	11	−1.2
700 (2 Hz)		0.45	15	−4.1

streak spacing. The motion in the Stokes layer creates a relative displacement between the streaks and the streamwise vortices, which lie between $10 < y^+ < 50$. The results obtained here return drag reduction as long as $\delta_{st}^+ < 8$, while an increase in drag is observed for values of δ_{st}^+ above 11, which agrees with the above statement from the work of Baron and Quadrio (1995).

C. Reynolds stress and turbulence production

The behavior of the Reynolds stresses $\langle u_i' u_j' \rangle$ for the two cases representing highest drag reduction ($T_{osc}^+ = 94$) and drag increase ($T_{osc}^+ = 700$) is compared with the conditions encountered for the stationary wall, where normalization is performed with u_τ of the stationary wall. For the oscillations at $T_{osc}^+ = 94$, the normal stress in the streamwise direction $\langle u'u' \rangle^+$ is lowered, with a peak reduction of 23%. A large relative reduction is also observed in the normal stress along the wall-normal direction $\langle v'v' \rangle^+$ by 14% and the shear stress $\langle u'v' \rangle^+$ by 18% (Fig. 6). Aside from the peak reduction, the streamwise fluctuations are reduced throughout the turbulent boundary layer, indicating that the effect of the oscillating wall is felt away from the wall up to approximately 200 y^+. The reduction of streamwise fluctuations is a consequence of the decreased wall-normal motions, dominated by ejections and sweeps. The spanwise

displacement between the streaks and the streamwise vortices produced by the Stokes layer inhibits the lift-up mechanism essential for maintaining turbulent energy production.

Apart from the reduction in the peak of the streamwise stress, the position of the peak is shifted toward larger wall-normal distance, where the shift is $4y^+$ for $\langle u'u' \rangle^+$, $23y^+$ for $\langle u'v' \rangle^+$, and $36y^+$ for $\langle v'v' \rangle^+$. For the oscillations at $T_{osc}^+ = 700$, a slight increase in all the components of Reynolds stress for the region corresponding to y^+ of 7–50 is observed (Fig. 6). The results of Choi et al. (1998) also report large reductions (30%) in the streamwise velocity fluctuations in the near-wall region for the oscillated wall, while the outer region remains unaltered by the presence of the oscillations, in agreement with that reported by Choi et al. (1998).

The dominant term of the turbulent kinetic energy production is evaluated from the measured data. The pre-multiplied normalized production ($P^+ y^+ = -\frac{\nu}{u_\tau^4} \overline{u'v'} \frac{\partial u}{\partial y} y^+$) is shown for oscillations at $T_{osc}^+ = 94$ and 700 in comparison with that of the stationary wall. For $T_{osc}^+ = 94$, a significant reduction in peak pre-multiplied production of 20% is observed at a wall-normal distance of $10 - 25y^+$, close to the peak reduction in the streamwise Reynolds normal stress (Fig. 6). A clear reduction is also observed upto $y^+ = 100$, corresponding to the region where hairpin vortices exist. For $T_{osc}^+ = 700$,
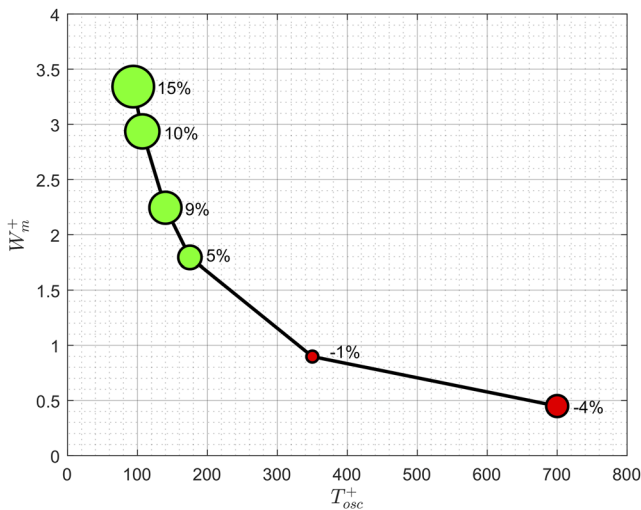

FIG. 5. Drag reduction as a function of oscillation frequency and wall velocity (experimental data obtained at $A^+ = 100$). Green for reduction and red for increase.
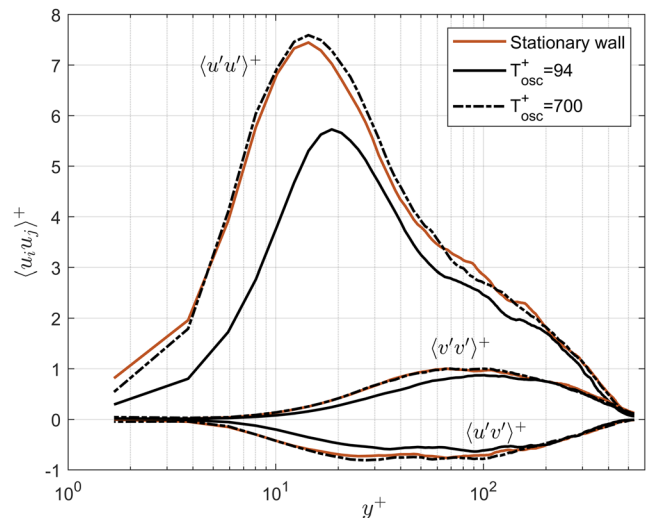

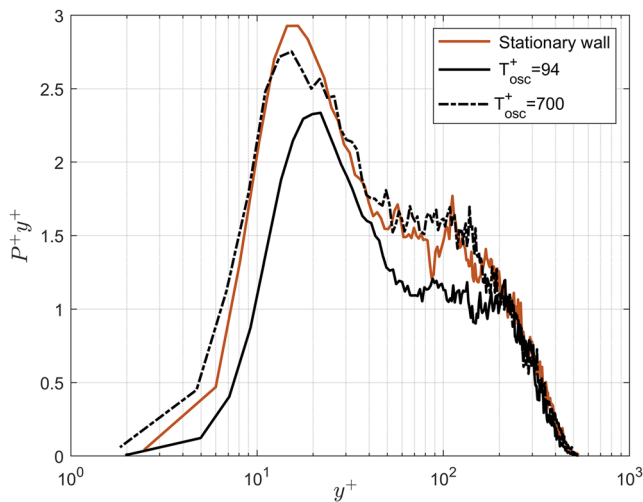**FIG. 6**. Comparison of the Reynolds stress distribution.

FIG. 7. Comparison of pre-multiplied turbulence production distribution.

FIG. 8. A sample of the instantaneous vorticity field obtained with stationary wall. Multimedia view: https://doi.org./10.1063/5.0015359.1

a mild decrease in pre-multiplied production occurs for y^+ up to 25 (Fig. 7), beyond which an increase is quantified. The oscillations at $T_{osc}^+ = 700$ are not sufficient to provide the required displacements of the streaks that leads to a reduction of the ejection and sweep events. Due to the lower time scale of these oscillations, additional disturbances are imparted in the flow field, which manifest as an increase in drag. Because of the small variation in the Reynolds stresses and TKE production (less than 2.5% in peak increase), the instantaneous flow organization is only analyzed considering the stationary wall and oscillations at $T_{osc}^+ = 94$, which resulted in the most reduction in drag.

D. Instantaneous flow organization

The observation of coherent motions in the boundary layer is performed here taking into account the topology of vorticity fluctuations ($\omega_z^+ = \frac{\omega_z \nu}{u_\tau^2}$ from planar PIV) and the combination of velocity fluctuations with vortex detection (L2-criterion from the tomographic PIV data). Attention is put on the role of groups of hairpins (hairpin packets, Adrian et al., 2000), which contribute significantly to the wall-normal momentum transport by focused ejections and sweep motions. For the initial observation of the presence and behavior of these structures, vorticity contours derived from the planar PIV data are used. The instantaneous structure of the vorticity field is scrutinized to determine the changes in the large-scale flow structures produced by wall oscillations (at $T_{osc}^+ = 94$ and $Z_{osc}^+ = 100$) with respect to those of the stationary wall.

The inspection of a series of instantaneous vorticity fields allows the identification of several recurrent flow events for the case of a stationary and oscillating wall. Figure 8 (Multimedia view) depicts as an example the vorticity contours of instantaneous structures typically observed. A series of visualizations is annexed in Fig. 8 (Multimedia view). For the discussion, boxed areas outline different flow features, numbered from 1 to 4 containing, respectively: (1) regions of high shear close to the wall due to the no-slip condition; (2) inclined vorticity sheet structures, lifted-up from the wall region;
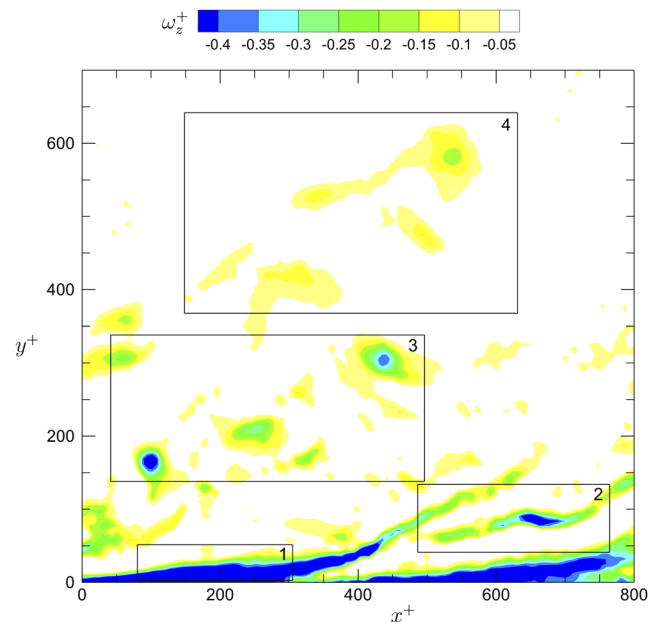
(3) hairpin heads featuring a localized peak of vorticity—the structure of a packet may be inferred too, with inclination to the wall between 25 and 45 (Adrian et al., 2000); and (4) weaker vorticity signatures in the outer regions of the boundary layer ($y^+ > 300$), featuring a remnant structure of decaying large scale hairpin-like motions.

Following the parameters extracted from the statistical analysis (streamwise velocity gradient at the wall, trends of Reynolds shear stress, and turbulent kinetic energy), spanwise wall oscillations at the optimum oscillating frequency and amplitude appear to simultaneously reduce skin-friction, the turbulence production, and the wall-normal velocity fluctuations. The following analysis focuses on the organization of the coherent flow structures under these conditions.

A hairpin packet features the presence of multiple hairpin vortices with their heads aligned approximately along a 30°-slope from the wall and separated by ~120–160 wall-units in the streamwise direction (Adrian et al., 2000). The hairpins appear atop the low-speed streaks where they tend to autogenerate, which leads to the packets (Zhou et al., 1999). In the present experiments, it is observed that for the stationary wall, hairpin packets are observed to be most frequently composed of 3–5 vortices typically separated by 50–150 wall units.

A marked difference is found for the case of the oscillating wall, where the hairpins appear more frequently as isolated or in pairs, packets with more than two hairpins being only seldom observed. Figure 9 (Multimedia view) displays a sequence of vorticity measurements for the stationary and oscillating wall.

The smaller size of the hairpin packets observed in the boundary layer developing over the oscillating wall is ascribed to the rapid
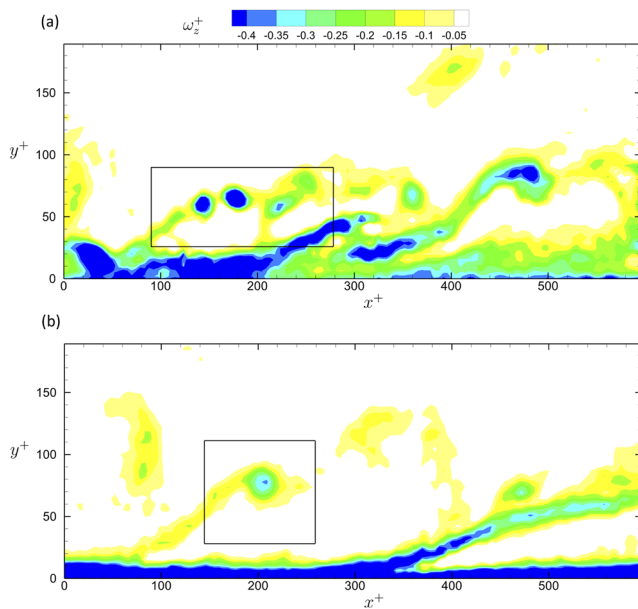
FIG. 9. Instantaneous spanwise vorticity distribution up to $y^+ = 200$, revealing a compact arrangement of hairpins (packet signature) for the stationary wall (a) and separated structures for the oscillating wall (b). Multimedia view: https://doi.org./10.1063/5.0015359.2

FIG. 10. Schematic illustration of the wall oscillations time diagram and indication of hairpin packet formation time.

sideways motion of the wall affecting the flow structure underneath the hairpins. It is hypothesized that the sudden shift of the low- and high-speed streaks beneath the hairpins inhibits the auto-generation of vortices as a result of the relative lateral shift between the preceding hairpin and the newly forming one. For a stationary wall, the presence of the leading hairpin and its induced ejection leads to the formation of a following structure, resulting in the continuous growth of the hairpin packet (Zhou *et al.*, 1999; Jodai and Elsinga, 2016). Figure 10 provides an illustration that combines the timing diagram of the spanwise oscillatory motion of the wall $Z(\phi)$, with a qualitative indication of hairpin formation and auto-generation period (t_{auto}^+). Given the linear relation between time and the oscillation phase ϕ, the latter is used in the remainder to refer to a specific condition within the oscillatory motion. The inhibition of auto-generation is expected to be most effective during the time interval of maximum wall velocity (red region in Fig. 10), whereas during the time of motion inversion (green region), the low wall velocity produces a situation similar to the stationary case. Based on the above, the dynamic behavior in the regime of wall oscillations is expected to display hairpins mostly generated during the period of minimum lateral velocity (motion inversion, the green region in Fig. 10). For an oscillating frequency of 15 Hz, which corresponds to a $T_{osc}^+ \approx 100$ (16.6 ms), the motion inversion time corresponds to a $t^+ = 23$. The latter is shorter than the auto-generation time $t_{auto}^+ \sim 30$ reported in the study of Jodai and Elsinga (2016) who estimated it from tomographic PIV measurements in a completely turbulent environment. Zhou *et al.* (1999) studied the case of auto-generation by observing the development of an initial perturbation to laminar flow with a mean turbulent velocity profile. In their work, values of t^+ one order
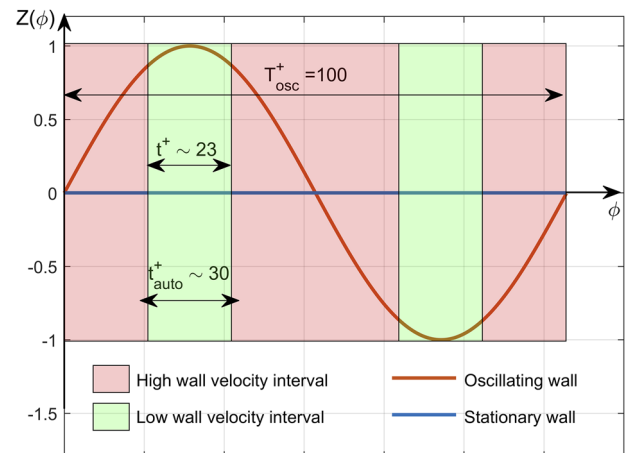
of magnitude larger are reported compared to the observations in the turbulent regime. The time spent during motion inversion of the current experiments corresponds to approximately that taken for the auto-generation of a single hairpin, which possibly explains the occurrence of single hairpins or, at most, hairpin pairs in a packet.

Following the stage of motion inversion, the high rate of lateral shift causes the fluid adjacent to the wall (streaks) to move with it as discussed by Touber and Leschziner (2012). The lower end of the hairpin vortices (legs) and particularly the newly generated hairpin is most affected by the lateral displacement as these parts are displaced away from the preceding hairpins and their induced ejection (low-speed region). This circumstance interrupts the auto-generation mechanism until the subsequent point of inversion when another low-velocity period allows auto-generation to some degree.

E. Tomographic PIV flow visualizations

The tomographic measurement volume encompasses primarily the buffer layer ($y^+ = 20$–70, Sec. III A). Visualizations of the streamwise velocity distribution close to the stationary wall [$y^+ = 20$, Fig. 11(a)] return the streaky pattern as a series of elongated low-speed regions with spanwise separation of ~100 wall units and a length varying from 600 to more than 850 wall units (current streamwise extent of the measurement domain). In agreement with the values widely reported in the literature (Kline *et al.*, 1967; Smith and Metzler, 1983; and Kähler, 2004). Increasing the distance from the wall up to $y^+ = 80$ [Fig. 11(b)], the streamwise coherence of the streaks diminishes and these regions appear as wider and often interrupted. Also, these observations agree with the study of Jodai and Elsinga (2016), which indicates that the velocity fluctuations in these two regions are governed by different structures and they are convected at different speeds (Del Álamo and Jiménez, 2009).

The inspection of the streamwise velocity contours at a wall-normal height of $y^+ = 20$ for the stationary and the oscillating wall at $Z(\phi) = 0$ [$\phi = 0, \pi$, Fig. 12 (Multimedia view)] shows that oscillations lead to a significant weakening of the streamwise coherence of
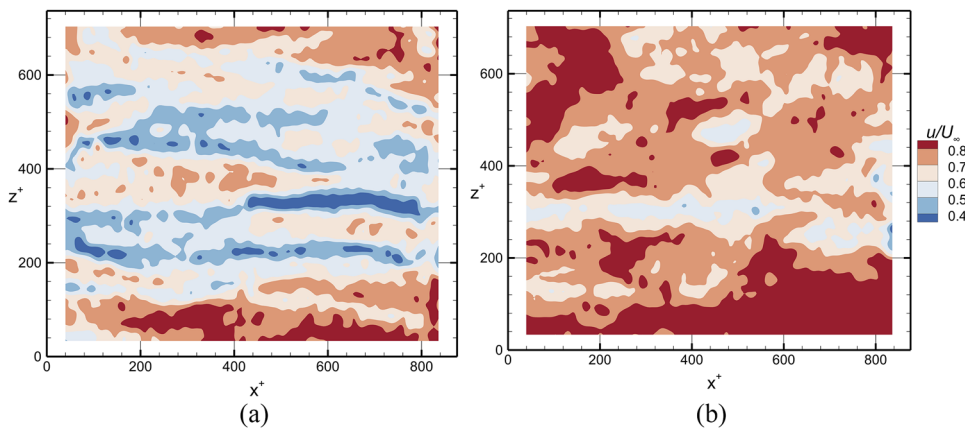
FIG. 11. Streamwise velocity contours at two wall-normal distances, $y^+ = 20$ (a) and 80 (b).

the streaks, with elongated low-velocity regions being more prominent for the stationary wall case. There are also regions within the field of view, which are devoid of streaks for the oscillating wall [Fig. 12(b) (Multimedia view)], which has been also observed in the DNS study of Touber and Leschziner (2012). A thorough inspection of the occurrence of this flow phenomenon is possible in the series of visualizations of the velocity contours annexed in Fig. 12 (Multimedia view). However, the DNS studies of oscillating wall (Touber and Leschziner, 2012) do not discuss the mechanism of drag reduction from the perspective of the hairpin packets. Rather, the drag reduction is ascribed to the weakening of the streaks. While the latter are important in near wall turbulence, their connection with the Reynolds shear stress, i.e., the turbulence contribution to the drag is weak, or indirect, at least. This can be inferred from the fact that the streamwise velocity fluctuations associated with the streaks are confined to a region very close to the wall ($y^+ \sim 15$), while the Reynolds shear stress peaks at a larger wall normal distance (Fig. 4). Hairpins and packets, however, are correlated with Reynolds stresses (Ganapathisubramani et al., 2003), hence turbulent drag. Hence, the development of hairpins (possibly from the streaks) provides a link between streak strength reduction very close to the wall and the reduction in Reynolds stresses farther from the wall.

A sample of the three-dimensional organization of vortices (iso-surface of the λ_2-criterion) and positive wall-normal velocity fluctuations v' is shown in Fig. 13 (Multimedia view), along with the streamwise velocity u distribution over a plane at position $y^+ = 20$, which identifies the high- and the low-speed regions. The flow field for the stationary wall case [Fig. 13(a) (Multimedia view)] features several elongated regions with wall-normal velocity fluctuations (purple) surrounded by multiple vortical structures (green) enclosed in boxes [1–6 in Fig. 13(a) (Multimedia view)]. This arrangement is in accordance with the concept of the hairpin packets, where the primary hairpin vortex being formed develops downstream and gives rise to a secondary hairpin vortex (Adrian, 2007). This mechanism is ascribed to the interaction of the low-speed fluid in the streak [shown in purple in Fig. 13 (Multimedia view)] that is ejected between the legs of the hairpin with the high-speed fluid above the legs causing the roll-up, in turn forming an arch-like structure (Zhou et al., 1999; Jodai and Elsinga, 2016). The supplementary material provided in Fig. 13 (Multimedia view) illustrates in a more extended way the above experimental observations for the stationary and oscillating wall. For the oscillating wall, the data at $\phi = 0$ and $\phi = \pi$ are shown. In the sample showing the instantaneous flow field for the oscillating wall [Fig. 13(b) (Multimedia view)],
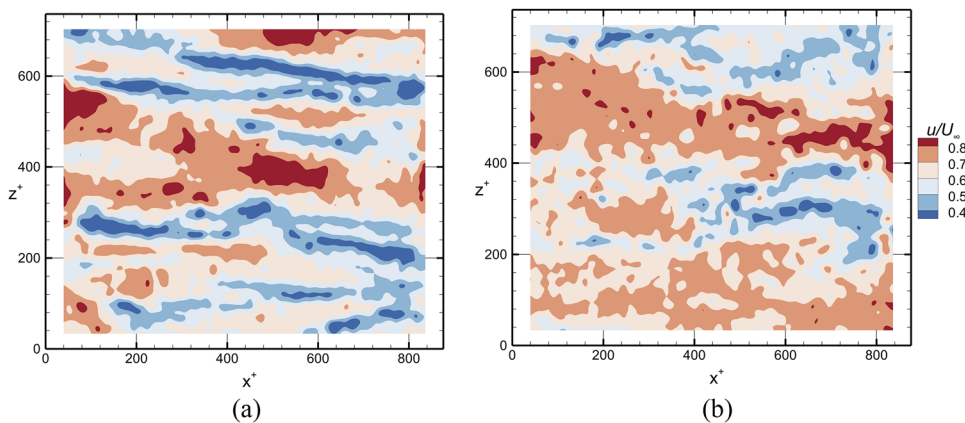

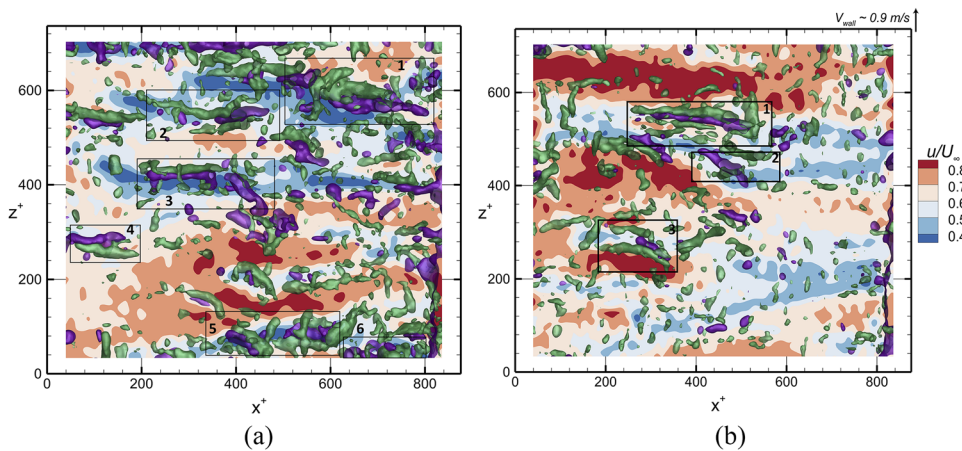**FIG. 12**. Streamwise velocity contours over a stationary (a) and oscillating wall (b) at wall-normal distance of $y^+ = 20$. Multimedia view: https://doi.org./10.1063/5.0015359.3

FIG. 13. 3D visualization of tomographic-PIV data over a stationary (a) and oscillating wall (b); isocontours of λ_2 = −20 000 [1/s²] (green) and $v = 0.1U_\infty$ (purple) at $y^+ = 20$. Multimedia view: https://doi.org/10.1063/5.0015359.4

the presence of wall-normal velocity fluctuations is significantly smaller. The low-speed flow regions are less pronounced [Fig. 13(b) (Multimedia view)], in turn inhibiting the process of hairpin formation and auto-generation. The organization of vortical structures [Fig. 13 (Multimedia view), enclosed in boxes] above the oscillating wall [1–3 in Fig. 13(b) (Multimedia view)] features mostly a streamwise orientation, which are significantly sparser when compared to the stationary wall. Moreover, arch-like structures appear less frequently and seldom arranged into packets. This further inhibits hairpin formation, since isolated hairpins need to be much stronger to initiate auto-generation as compared to hairpins in a packet, which can be weak and still trigger auto-generation (Goudar et al., 2016). Such strong hairpins have a very low probability.

Statistical evidence of this effect can be gathered considering the flow enstrophy ω^2 as an overall measure of the vorticity fluctuations over the domain of observation ($20 < y^+ < 80$). The mean value of ω^2 is 1.98×10^4 s^{-2} for the stationary wall, whereas, while for the oscillating wall, it reduces to 1.54×10^4 s^{-2} at $\phi = 0, \pi$ (maximum velocity). A slightly higher value ($\omega^2 = 1.65 \times 10^4$ s^{-2}) is observed during motion inversion ($\phi = \pi/2, 3\pi/2$), indicating that the turbulent properties also depend upon the phase of the oscillatory motion. The latter correlates with the reduction in vortical structures described earlier and is consistent with the proposed mechanism of auto-generation inhibition. Albeit for a different geometry (circular pipe flow), Coxe et al. (2019) performed a DNS study, proposing a phase dependence of vorticity fluctuations with transverse wall oscillations too.

The proposed model for the effect of wall oscillation on hairpin packet formation is graphically conceptualized in the schematics of Fig. 14. The autogeneration of the hairpin packet is sketched for the stationary wall (Fig. 14, top), where the blue region corresponds to the low-speed streak, which is lifted up. The ejection is intensified as the hairpin packet grows in size, with the current illustration depicting the formation of a packet of three hairpins (1–3 in Fig. 14—stationary wall). For the oscillating wall (Fig. 14—oscillating wall), an initial hairpin (1, Fig. 14—oscillating wall) cannot autogenerate downstream due to the rapid lateral shift of the trailing flow region at a lower distance from the wall. The transverse wall motion also distorts the streaks; however, this is not regarded as the main

inhibition factor compared to the increased distance between the focused ejection from the preceding hairpin vortex and the trailing region. In turn, the formation and growth of the trailing hairpin (2, Fig. 14—oscillating wall) will occur independently and without the accelerating effect of autogeneration. As a result, the pattern of isolated hairpins reduces the collective focused ejection of the low-speed fluid, with a significant reduction of momentum mixing, which directly translates into a reduction in skin-friction drag.
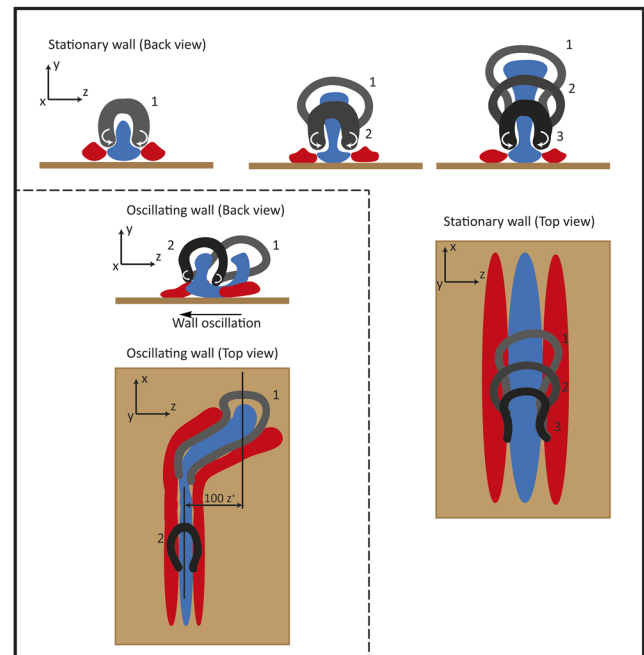

FIG. 14. Illustration of hairpin autogeneration for stationary and oscillating wall [red—high-speed streaks, blue—low-speed streaks, and shades of gray used to represent different hairpins and are numbered (1, 2, 3)].

IV. CONCLUSIONS

The response of a turbulent boundary layer developing over a spanwise oscillating wall has been studied experimentally employing planar and tomographic PIV. High-resolution planar PIV allowed us to accurately measure the wall shear stress directly from the velocity profile down to a wall-normal distance of $y^+ = 2$. A maximum drag reduction of 15% is quantified for the oscillating wall at $T_{osc}^+ = 94$ and $A_{osc}^+ = 100$ when compared to the stationary wall. The reductions obtained are found to be in agreement with the previously reported DNS studies. A significant reduction of turbulent stresses and pre-multiplied turbulent kinetic energy production is found up to $y^+ = 100$. The instantaneous vorticity fields visualized in the planar and tomographic-PIV measurements reveal marked differences between the stationary and the oscillating wall. Planar data provide evidence through the visualizations of the cross-sectional footprints of these highly three-dimensional coherent structures. A hypothesis is forwarded to provide an explanation for the observed reduction in near-wall vorticity and accompanying reduction of the number of hairpins in a hairpin packet when the wall is oscillated. According to the proposed mechanism and existing literature on hairpin packet generation, the oscillation frequency may be associated with the size of the packet, whereas the amplitude of oscillation needs to be at least as large as the streaks spanwise separation to be effective. In line with this model, the hairpin packet formation depends on the motion of the oscillating wall and as such on the phase in the oscillation cycle. Quantitative information from the tomographic PIV data supports this assumption, where the enstrophy in the field reduces by 22% for the oscillating wall at $\phi = 0, \pi$ and by 16.7% for the oscillating wall at $\phi = \pi/2, 3\pi/2$.

ACKNOWLEDGMENTS

DATA AVAILABILITY

The data that support the findings of this study are openly available in 4TU. Research data at doi:10.4121/uuid:ef50c4a7-1c32-4072-be1c-02782176fa2d.

REFERENCES

Adrian, R. J., "Dynamic ranges of velocity and spatial resolution of particle image velocimetry," Meas. Sci. Technol. **8**(12), 1393 (1997).

Adrian, R. J., "Hairpin vortex organization in wall turbulence," Phys. Fluids **19**(4), 041301 (2007).

Adrian, R. J., Meinhart, C. D., and Tomkins, C. D., "Vortex organization in the outer region of the turbulent boundary layer," J. Fluid Mech. **422**, 1–54 (2000).

Adrian, R. J. and Westerweel, J., *Particle Image Velocimetry* (Cambridge University Press, 2011).

Baron, A. and Quadrio, M., "Turbulent drag reduction by spanwise wall oscillations," Appl. Sci. Res. **55**(4), 311–326 (1995).

Boutier, A., Pagan, D., and Soulevant, D., "Measurements accuracy with 3D laser velocimetry," NASA STI/Recon Technical Report No. A 86, 1985.

Choi, K.-S., "Near-wall structure of turbulent boundary layer with spanwise-wall oscillation," Phys. Fluids **14**(7), 2530–2542 (2002).

Choi, K.-S., DeBisschop, J.-R., and Clayton, B. R., "Turbulent boundary-layer control by means of spanwise-wall oscillation," AIAA J. **36**(7), 1157–1163 (1998).

Choi, J.-I., Xu, C.-X., and Sung, H. J., "Drag reduction by spanwise wall oscillation in wall-bounded turbulent flows," AIAA J. **40**(5), 842–850 (2002).

Christensen, K. T. and Adrian, R. J., "Statistical evidence of hairpin vortex packets in wall turbulence," J. Fluid Mech. **431**, 433 (2001).

Coxe, D., Peet, Y., and Adrian, R. J., "Vorticity statistics and distributions in drag reduced turbulent pipe flow with transverse wall oscillations," in *11th International Symposium on Turbulence and Shear Flow Phenomena, TSFP* (TSFP, 2019).

Del Álamo, J. C. and Jiménez, J., "Estimation of turbulent convection velocities and corrections to Taylor's approximation," J. Fluid Mech. **640**, 5–26 (2009).

Di Cicca, G. M., Iuso, G., Spazzini, P. G., and Onorato, M., "Particle image velocimetry investigation of a turbulent boundary layer manipulated by spanwise wall oscillations," J. Fluid Mech. **467**, 41–56 (2002).

Driver, D. M. and Hebbar, S. K., "Experimental study of a three-dimensional, shear-driven, turbulent boundary layer," AIAA J. **25**(1), 35–42 (1987).

Elsinga, G. E., Scarano, F., Wieneke, B., and van Oudheusden, B. W., "Tomographic particle image velocimetry," Exp. Fluids **41**(6), 933–947 (2006).

Gad-el-Hak, M., "Modern developments in flow control," Appl. Mech. Rev. **49**(7), 365–379 (1996).

Gan, L., Cardesa-Duenas, J. I., Michaelis, D., and Dawson, J. R., "Comparison of tomographic PIV algorithms on resolving coherent structures in locally isotropic turbulence," in *16th International Symp on Applications of Laser Techniques to Fluid Mechanics* (TSFP, Lisbon, Portugal, 2012).

Ganapathisubramani, B., Longmire, E. K., and Marusic, I., "Characteristics of vortex packets in turbulent boundary layers," J. Fluid Mech. **478**, 35–46 (2003).

Ghaemi, S. and Scarano, F., "Multi-pass light amplification for tomographic particle image velocimetry applications," Meas. Sci. Technol. **21**(12), 127002 (2010).

Goudar, M. V., Breugem, W.-P., and Elsinga, G. E., "Auto-generation in wall turbulence by the interaction of weak eddies," Phys. Fluids **28**(3), 035111 (2016).

Howard, R. J. A. and Sandham, N. D., "Simulation and modelling of a skewed turbulent channel flow," Flow, Turbul. Combust. **65**(1), 83–109 (2000).

Jodai, Y. and Elsinga, G. E., "Experimental observation of hairpin auto-generation events in a turbulent boundary layer," J. Fluid Mech. **795**, 611–633 (2016).

Jung, W. J., Mangiavacchi, N., and Akhavan, R., "Suppression of turbulence in wall-bounded flows by high-frequency spanwise oscillations," Phys. Fluids A **4**(8), 1605–1607 (1992).

Kähler, C. J., "The significance of coherent flow structures for the turbulent mixing in wall-bounded flows," Ph.D. dissertation (DLR, Dt. Zentrum für Luft-und Raumfahrt, 2004).

Kähler, C. J., Scholz, U., and Ortmanns, J., "Wall-shear-stress and near-wall turbulence measurements up to single pixel resolution by means of long-distance micro-PIV," Exp. Fluids **41**(2), 327–341 (2006).

Kline, S. J., Reynolds, W. C., Schraub, F. A., and Runstadler, P. W., "The structure of turbulent boundary layers," J. Fluid Mech. **30**(4), 741–773 (1967).

Laadhari, F., Skandaji, L., and Morel, R., "Turbulence reduction in a boundary layer by a local spanwise oscillating surface," Phys. Fluids **6**(10), 3218–3220 (1994).

Lima Pereira, L. T., Ragni, D., Avallone, F., and Scarano F., "Pressure fluctuations from large-scale PIV over a serrated trailing edge," Exp. Fluids **61**(3), 71 (2020).

Lozano-Durán, A., Flores, O., and Jiménez, J., "The three-dimensional structure of momentum transfer in turbulent channels," J. Fluid Mech. **694**, 100 (2012).

Monty, J. P., Hutchins, N., Ng, H. C. H., Marusic, I., and Chong, M. S., "A comparison of turbulent pipe, channel and boundary layer flows," J. Fluid Mech. **632**, 431–442 (2009).

Quadrio, M. and Ricco, P., "Critical assessment of turbulent drag reduction through spanwise wall oscillations," J. Fluid Mech. **521**, 251–271 (2004).

Quadrio, M. and Sibilla, S., "Numerical simulation of turbulent flow in a pipe oscillating around its axis," J. Fluid Mech. **424**, 217–241 (2000).

Robinson, S. K., "Coherent motions in the turbulent boundary layer," Annu. Rev. Fluid Mech. **23**, 601–639 (1991).

Ricco, P. and Quadrio, M., "Wall-oscillation conditions for drag reduction in turbulent channel flow," Int. J. Heat Fluid Flow **29**(4), 891–902 (2008).

Scarano, F., "Theory of non-isotropic spatial resolution in PIV," Exp. Fluids **35**(3), 268–277 (2003).

Scarano, F., "Tomographic PIV: Principles and practice," Meas. Sci. Technol. **24**(1), 012001 (2012).

Scarano, F. and Poelma, C., "Three-dimensional vorticity patterns of cylinder wakes," Exp. Fluids **47**(1), 69 (2009).

Scarano, F. and Riethmuller, M. L., "Advances in iterative multigrid PIV image processing," Exp. Fluids **29**(7), S051–S060 (2000).

Schlatter, P. and Örlü, R., "Assessment of direct numerical simulation data of turbulent boundary layers," J. Fluid Mech. **659**, 116–126 (2010).

Schlichting, H. and Gersten, K., *Boundary-layer Theory* (Springer, 2016).

Sendstad, O. and Moin, P., "The near wall mechanics of three-dimensional turbulent boundary layers," Technical Report No. TF-57, 1992.

Smith, C. R. and Metzler, S. P., "The characteristics of low-speed streaks in the near-wall region of a turbulent boundary layer," J. Fluid Mech. **129**, 27–54 (1983).

Touber, E. and Leschziner, M. A., "Near-wall streak modification by spanwise oscillatory wall motion and drag-reduction mechanisms," J. Fluid Mech. **693**, 150–200 (2012).

Vila, C. S., Vinuesa, R., Discetti, S., Ianiro, A., Schlatter, P., and Örlü, R., "On the identification of well-behaved turbulent boundary layers," J. Fluid Mech. **822**, 109–138 (2017).

Vukoslavcevic, P., Wallace, J. M., and Balint, J.-L., "The velocity and vorticity vector fields of a turbulent boundary layer. Part 1. Simultaneous measurement by hot-wire anemometry," J. Fluid Mech. **228**, 25–51 (1991).

Wieneke, B., "Volume self-calibration for 3D particle image velocimetry," Exp. Fluids **45**(4), 549–556 (2008).

Zhou, J., Adrian, R. J., Balachandar, S., and Kendall, T. M., "Mechanisms for generating coherent packets of hairpin vortices in channel flow," J. Fluid Mech. **387**, 353–396 (1999).